7-1-1995

The *Hubble Space Telescope* Sample of Radio-loud Quasars: Ultraviolet Spectra of the First 31 Quasars

Beverley J. Wills
University of Texas at Austin

Keith L. Thompson
University of Texas at Austin

Mingsheng Han
University of Texas at Austin

H. Netzer
Tel Aviv University, Israel

D. Wills
University of Texas at Austin

See next page for additional authors

Authors
Beverley J. Wills, Keith L. Thompson, Mingsheng Han, H. Netzer, D. Wills, J. A. Baldwin, Gary J. Ferland, I W. A. Browne, and M. S. Brotherton

The *Hubble Space Telescope* Sample of Radio-loud Quasars: Ultraviolet Spectra of the First 31 Quasars

Notes/Citation Information
Published in *The Astrophysical Journal*, v. 447, no. 1, p. 139-158.

Digital Object Identifier (DOI)
http://dx.doi.org/10.1086/175861

THE ASTROPHYSICAL JOURNAL, 447:139–158, 1995 July 1

THE *HUBBLE SPACE TELESCOPE* SAMPLE OF RADIO-LOUD QUASARS: ULTRAVIOLET SPECTRA OF THE FIRST 31 QUASARS[1]

BEVERLEY J. WILLS,[2] KEITH L. THOMPSON,[2] MINGSHENG HAN,[2,3] H. NETZER,[4] D. WILLS,[2]
J. A. BALDWIN,[5] G. J. FERLAND,[6] I. W. A. BROWNE,[7] AND M. S. BROTHERTON[2]
Received 1994 January 21; accepted 1994 March 17

ABSTRACT

We report the first results from a continuing program to investigate the multifrequency spectrophotometric and other properties of a sample of about 50 radio-loud quasars in the redshift range $\sim$0.3–1.3. Here we present spectrophotometric data of high signal-to-noise ratio ($\gtrsim$20 in the continuum) of the first 31 radio-loud quasars, over the wavelength range from below Lyα to an observed wavelength of 3250 or 4800 Å, obtained using the Faint Object Spectrograph on the *Hubble Space Telescope*. We have also made quasi-simultaneous observations to extend these spectra beyond the Balmer lines—either Hβ or Hα—and those data will be presented in companion papers. In the ultraviolet and optical, the resolution is 300–400 km s^{-1} and in the infrared, about 1000 km s^{-1}. The sample was selected by luminosity of the extended radio emission, and to cover a range of radio core-dominance, in order to test ideas relating to orientation of the continuum and emission-line regions to the observer's line of sight.

We present the ultraviolet spectra, and tabulate basic spectroscopic measurements: continuum flux densities and spectral indices, intensities and equivalent widths for all strong emission lines after deblending, as well as profile parameters such as various line widths and asymmetries. The relations between these and other parameters will be presented in detail in a later paper.

In our low-redshift sample we have good coverage from C III λ977 to O VI λ1035, a region that is very confused by Lyman forest absorption in high-redshift quasars observed from the ground. We find that Lyβ is less than 10% of the strength of O VI λ1035. The ratio O VI λ1035/Lyα $\sim$0.21 supports photoionization models with high ionization and a small, dense broad-line region, although the weakness of C III λ977—typically 5% of Lyα—limits the amount of gas with densities $\gtrsim 10^{10}$–10^{11} cm^{-3}. The N III λ991 line is present at about 4% the strength of Lyα.

In contrast to the lobe-dominant quasars, which have flat ultraviolet-optical continua (in F_ν), all quasars with steep continua are radio core-dominant, and their broad lines tend to have lower equivalent width. Associated absorption is more prominent in the lobe-dominant quasars. Both these results are consistent with unified schemes in which a synchrotron-emitting jet is viewed at small angles to the line-of-sight in core-dominant quasars, and the line-of-sight at larger angles passes through cooler gas. In addition, we find and discuss significant differences in C IV λ1549 line asymmetries: the profiles of core-dominant quasars have stronger red wings, profiles of lobe-dominant quasars tend to be symmetric with both red and blue wings, and radio-quiet QSO profiles have stronger blue wings.

Subject headings: line: profiles — quasars: emission lines — quasars: general — radio sources: general

1. INTRODUCTION

The *International Ultraviolet Explorer* with its 45 cm telescope and rugged, low-resolution (FWHM $\sim$ 1000 km s^{-1}) spectrographs, for 14 years led the investigation of ultraviolet spectra of low-redshift AGNs (Kondo 1987). For the first time, their strong resonance lines became accessible (Lyα, C IV, N V, Si IV, Mg II, etc.), as well as the high-energy (ionizing) continuum, hitherto seen only in high-redshift QSOs. The "Lyα/Hβ problem" was established and investigated; the problem of the great strengths of low-ionization lines (e.g., Fe II) relative to the ionizing continuum was revealed (e.g., Netzer 1985); and the importance of reddening was questioned. There were tantalizing hints of differences in broad line widths and redshifts within individual spectra. All these indicated a more complex structure in the inner regions of the most luminous AGNs. In addition, it was becoming clear that the radio jets defined an axis of symmetry for the central engine, raising the question of how the structure of the continuum and emission-line regions might be related to this fundamental direction. Further progress required the comparison of line profiles of the strong and weak UV lines with improved signal-to-noise ratio and wavelength resolution. The Faint Object Spectrograph on board the *Hubble Space Telescope*, with improved resolution (230–350 km s^{-1} FWHM) and light-gathering power, now provides this capability—as well as the capability of observing fainter QSOs,

[1] Based on observations with the NASA/ESA *Hubble Space Telescope*, obtained at the Space Telescope Science Institute, which is operated by the Association of Universities for Research in Astronomy, Inc., under NASA contract NAS 5-26555.

[2] McDonald Observatory and Department of Astronomy, University of Texas at Austin, Austin, TX 78712.
[3] Now at the Department of Astronomy, University of Wisconsin-Madison, Madison, WI 53706.
[4] Department of Physics and Astronomy, Tel Aviv University, Tel Aviv 69978, Israel.
[5] Cerro Tololo Inter-American Observatory, P.O. Box 26732, Tucson, AZ 85726.
[6] Department of Physics and Astronomy, University of Kentucky, Lexington, KY 40506-0055.
[7] University of Manchester Nuffield Radio Astronomy Labs., Jodrell Bank, Macclesfield, Cheshire, SK11 9DL, England, UK.

hence allowing the observation of carefully defined samples. We are investigating such a sample, and this paper describes our initial measurements and some results.

The main observational goal of our *HST*-based program is to produce the definitive sample of spectra of ~50 radio-loud quasars, each over the rest wavelength from range below Lyα to beyond Hβ, enabling determination of the continuum over a wide wavelength range, and the comparison of the ultraviolet lines (e.g., Lyα, N v λ1240, λ1400, C iv λ1549, C iii] λ1909, Mg ii λ2798, Fe ii $\lambda\lambda$2000–3000) with, for example, hydrogen Balmer lines, He ii λ4686, Fe ii λ4570 and λ5300, etc. (and Paβ for a significant subset). Ultraviolet data obtained with the *Hubble Space Telescope's* Faint Object Spectrograph (*HST*'s FOS) are being complemented by quasi-simultaneous optical and infrared spectroscopy from McDonald Observatory, KPNO, UKIRT, and CTIO. This is the only large well-defined sample being observed by *HST* to investigate the intrinsic properties of QSOs. (We refer to radio-loud QSOs as "quasars").

A major goal of our program is to test the dependence of spectroscopic properties on inclination of the axis of the central engine (defined by the radio axis). We have therefore chosen our sample to cover a wide range of radio-core dominance—a measure of the inclination of the central engine's axis to the line of sight—while constraining the range in extended radio luminosity, which is inclination-*independent*. Thus the two great advantages of our data set are the wide wavelength range covering high- and low-ionization lines and a large part of the continuum, and its design to measure aspect dependence in a way free of luminosity bias.

Here we present the available data—31 spectra from *HST* Cycles 1 and 2 (observations begun in 1991 August). We have already used some of these spectral data to compare the strengths of ultraviolet and optical lines from the narrow-line region (NLR) (Wills et al. 1993a), and to compare the continuum and unusual emission-line spectrum of the blazar 3C 279 with fortuitously simultaneous gamma-ray observations with the Egret telescope on the *Compton Gamma Ray Observatory* (Netzer et al. 1994).

Subsequent papers will present further *HST* ultraviolet data, the optical and infrared data, and compare emission-line strengths, profiles and profile shifts, and continuum shape, and will use new and existing radio and X-ray data to investigate basic questions such as the structure of the broad-line region (BLR), the dependence of line strengths and ratios on luminosity (the Baldwin effect), the relations among IR, optical, UV and X-ray luminosity, etc., and so the sample will be used for investigating other spectroscopic ideas and problems besides the inclination dependence. The present sample will be a useful starting point for investigations by others—by extending the sample (1) to complete a 3CR sample, (2) to fainter optical limits, and (3) to different ranges in extended radio luminosity (e.g., radio galaxies), and (4) for comparison with radio-quiet samples.

The selection of the sample and the observations are described in §§ 2 and 3. The calibrations and corrections applied to the data are summarized briefly in § 4, and § 5 discusses continuum measurement, and line deblending and measurement. The results of line measurements are also presented in § 5—fluxes, equivalent widths, and line profile measurements for the strongest lines, as well as relative line strengths or upper limits for 16 lines commonly identified in the ultraviolet spectra of quasars. These sections are followed by a brief discussion of some results from this work (§ 6).

2. THE SAMPLE

Our Cycle 1 sample was originally a low-frequency flux-limited sample from the 3CR catalog with complete optical identifications, and $z < 1.8$, selected over a limited range of an orientation-independent property, the radio lobe luminosity, L_{ext}. The range of log L_{ext} is 26.5–27.6, where L_{ext} is calculated in ergs s^{-1} Hz^{-1} at 6 cm rest wavelength, assuming $q_0 = 0$, $H_0 = 50$ km s^{-1} Mpc^{-1}. This sample was supplemented by core-dominant quasars selected over the same L_{ext} interval. After *HST*'s spherical aberration was discovered, with consequent reduced throughput of the combined *HST* and FOS, the faintest quasars were replaced by brighter objects ($V \lesssim 18$), selected to retain sample size and to achieve the same scientific goals, with the same range in lobe luminosity, or selected as quasar pairs—a radio core- and a lobe-dominated quasar, each matched within 0.5 in log L_{ext}, and 0.2 in log z. Our sample consists of roughly equal numbers of lobe- and core-dominant quasars with a wide range in the ratio, R, of core to extended radio emission, from about 0.01 to 100 (at 6 cm rest wavelength) and a similar range in X-ray and radio core luminosity.

The choice of defining parameters has several advantages. The low L_{ext} favors small z. This means brighter quasars and therefore a more completely identified sample. They are easier to observe at ultraviolet, optical, IR, X-ray wavelengths, and have more information available from literature and other sources. The lower redshift also means better linear resolution for imaging, especially at radio wavelengths. The low redshifts also allow a comparison with AGNs of lower luminosity, for example, Seyfert 1 galaxies and broad-line radio galaxies. Because the quasars are relatively low redshift and radio loud, most, if not all, are expected to have *ROSAT* X-ray data.

Out of our sample of ~50, *HST* successfully observed 31 quasars in Cycles 1 and 2. In Cycle 3 only two were observed successfully, and we are observing the remainder in Cycle 4. Other *HST* programs have observed, or plan to observe, five other sources from our sample. These additional sources will have less certain photometric calibration as they use the 1″ aperture, and also will not all have quasi-simultaneous ground-based spectroscopy (although we are attempting this). Basic data for Cycle 1 and 2 objects are given in Tables 1 and 2.

3. OBSERVATIONS

A log of the observations is given in Table 1, including positions measured from the GSSS (Guide Star Selection System) survey plates (Lasker 1990), using the GSSS Astrometric Support Package at the Space Telescope Science Institute. These J2000 coordinates are in the GSSS reference frame used by *HST* and are internally accurate to ~0″.3–0″.5 rms. The table gives a brief description of the FOS configuration used, the observation date and exposure time, and an identifying "root" name as used in the *HST* archives. *HST*'s FOS is described in detail by Ford & Hartig (1990) and Kinney (1992).

We used the FOS high-resolution grating settings G130H, G190H, G270H, and G400H, centered at about 1350, 1950, 2750, and 4000 Å, respectively, to cover the wavelength range from below Lyα to above the atmospheric cutoff—to observed wavelengths of either ~3250 or ~4800 Å. The resolution of the spectrograph was ~1300. We used the Red- or Blue-side Digicon detectors as specified in Table 1. For each grating setup an electron image from a photocathode is magnetically focused onto a Digicon array of 512 diodes each 50 μm wide $\times$ 200 μm perpendicular to the dispersion direction. The elec-

TABLE 1

LOG OF *HST* OBSERVATIONS

Target	Alias	Plate Id	RA (2000)	DEC (2000)	Side	Grating	Exp.T (sec)	Date (UT)	Root
B2 0110+29	0110+297	00DV	01 13 24.21	29 58 15.8	RD	G190H	936	1992 Sep 06	Y12B0102T[a]
					RD	G270H	438	1992 Sep 06	Y12B0103T[a]
PKS 0112−01		00WT	01 15 17.12	−01 27 04.9	RD	G270H	918	1991 Sep 06	Y0PE0102T
					RD	G400H	732	1991 Sep 06	Y0PE0103T
3C 47.0	0133+207	00FG	01 36 24.47	20 57 26.5	RD	G190H	1884	1992 Aug 30	Y12B0202T
					RD	G270H	912	1992 Aug 30	Y12B0203T
PKS 0403−13		02NG	04 05 33.98	−13 08 14.1	RD	G190H	1410	1991 Oct 11	Y0PE0202T
					RD	G270H	756	1991 Oct 11	Y0PE0203T
					RD	G400H	534	1991 Oct 12	Y0PE0204T
3C 175	0710+118	02UV	07 13 02.39	11 46 15.5	RD	G190H	1092	1991 Dec 03	Y0PE0302T
					RD	G270H	720	1991 Dec 03	Y0PE0303T
					RD	G400H	486	1991 Dec 03	Y0PE0304T
3C 186	0740+380	031M	07 44 17.47	37 53 16.9	RD	G270H	1080	1991 Dec 03	Y0PE0402T
					RD	G400H	846	1991 Dec 03	Y0PE0403T
3C 207	0838+133	028H	08 40 47.56	13 12 23.7	RD	G190H	1254	1991 Dec 04	Y0PE0502T
					RD	G190H	1260	1991 Dec 04	Y0PE0503T
					RD	G270H	748	1991 Dec 04	Y0PE0504T
					RD	G270H	740	1991 Dec 04	Y0PE0505T
					RD	G400H	1230	1991 Dec 04	Y0PE0506T
PKS 0859−14		00FG	09 02 16.80	−14 15 31.1	RD	G270H	450	1993 Mar 05	Y12B0302T
3C 215	0903+169	0204	09 06 31.86	16 46 12.2	RD	G190H	1830	1992 May 01	Y0PE0602T
					RD	G190H	1830	1992 May 01	Y0PE0603T
					RD	G190H	1830	1992 May 01	Y0PE0604T
					RD	G270H	726	1992 May 01	Y0PE0605T
					RD	G270H	720	1992 May 01	Y0PE0606T
					RD	G400H	1134	1992 May 01	Y0PE0607T
3C 216.0	0906+430	021G	09 09 33.53	42 53 47.0	RD	G190H	1688	1992 Dec 28	Y12B0402T
					RD	G190H	1690	1992 Dec 28	Y12B0403T
					RD	G270H	818	1992 Dec 28	Y12B0404T
					RD	G270H	820	1992 Dec 29	Y12B0405T
B2 0923+39	0923+392	01BS	09 27 03.05	39 02 20.9	RD	G190H	2082	1991 Dec 27	Y0PE0702T[a]
					RD	G270H	1206	1991 Dec 27	Y0PE0703T[a]
					RD	G400H	1002	1991 Dec 27	Y0PE0704T[a]
					RD	G190H	2185	1993 Jan 24	Y1170102T
					RD	G270H	1206	1993 Jan 24	Y1170103T
					RD	G400H	1002	1993 Jan 24	Y1170104T
4C 55.17	0954+556	0009	09 57 38.16	55 22 57.7	RD	G190H	1928	1993 Jan 20	Y1170302T
					RD	G190H	1930	1993 Jan 20	Y1170303T
					RD	G270H	1650	1993 Jan 20	Y1170304T
PKS 1103−006		04I7	11 06 31.75	−00 52 53.4	RD	G190H	498	1992 Dec 29	Y12B0502T
					RD	G270H	240	1992 Dec 29	Y12B0503T
3C 254	1111+408	01QX	11 14 38.70	40 37 20.1	RD	G190H	1110	1992 Apr 15	Y0PE0802T
					RD	G190H	1110	1992 Apr 15	Y0PE0803T
					RD	G270H	1374	1992 Apr 15	Y0PE0804T
					RD	G400H	1152	1992 Apr 15	Y0PE0805T
PKS 1127−14		02MF	11 30 07.02	−14 49 27.6	RD	G270H	534	1993 Jan 01	Y12B0602T
3C 263	1137+660	01RM	11 39 57.06	65 47 49.5	RD	G190H	534	1991 Nov 06	Y0PE0902T
					RD	G270H	276	1991 Nov 06	Y0PE0903T
					RD	G400H	204	1991 Nov 06	Y0PE0904T
3C 277.1	1250+568	01R1	12 52 26.29	56 34 20.4	RD	G190H	1986	1991 Nov 02	Y0PE0A02T
					RD	G270H	1122	1991 Nov 02	Y0PE0A03T
					RD	G400H	864	1991 Nov 02	Y0PE0A04T
3C 279	1253−055	024R	12 56 11.15	−05 47 21.6	RD	G190H	1270	1992 Apr 08	Y0PE0B02T
					RD	G190H	1280	1992 Apr 08	Y0PE0B03T
					RD	G270H	1278	1992 Apr 08	Y0PE0B04T
					RD	G400H	918	1992 Apr 08	Y0PE0B05T
3C 288.1	1340+606	01R0	13 42 13.24	60 21 42.9	RD	G270H	884	1993 Apr 06	Y12B0702T
					RD	G270H	880	1993 Apr 06	Y12B0703T
PKS 1354+19	4C19.44	019M	13 57 04.48	19 19 06.5	RD	G190H	492	1993 Apr 29	Y12B0802T
					RD	G270H	222	1993 Apr 29	Y12B0803T
					RD	G400H	174	1993 Apr 29	Y12B0804T
3C 323.1	1545+210	0280	15 47 43.53	20 52 16.4	RD	G190H	384	1992 Apr 08	Y0PE0D02T

TABLE 1—*Continued*

Target	Alias	Plate Id	RA (2000)	DEC (2000)	Side	Grating	Exp.T (sec)	Date (UT)	Root
					RD	G270H	225	1992 Apr 08	Y0PE0D03T
					RD	G400H	156	1992 Apr 08	Y0PE0D04T
					BL	G130H	1150	1992 Apr 10	Y0PE0C02T
					BL	G130H	1160	1992 Apr 10	Y0PE0C03T
B2 1555+33	1555+332	01RN	15 57 29.95	33 04 46.7	RD	G270H	1018	1993 May 22	Y12B0902T
					RD	G270H	1010	1993 May 22	Y12B0903T
DA 406	1611+343	01RW	16 13 41.10	34 12 48.0	RD	G270H	876	1992 Apr 04	Y0PE0F02T
					RD	G400H	690	1992 Apr 04	Y0PE0F03T
3C 334	1618+177	01GC	16 20 21.80	17 36 23.9	RD	G190H	648	1991 Sep 07	Y0PE0G02T
					RD	G270H	345	1991 Sep 07	Y0PE0G03T
					RD	G400H	252	1991 Sep 07	Y0PE0G04T
OS 562	1637+574	00FG	16 38 13.46	57 20 23.9	RD	G190H	1314	1992 Aug 11	Y1170502T
					RD	G270H	564	1992 Aug 11	Y1170503T
					RD	G400H	450	1992 Aug 11	Y1170504T
3C 345	1641+399	00CL	16 42 58.78	39 48 36.9	RD	G190H	426	1992 Jun 07	Y0PE0I02T
					RD	G270H	225	1992 Jun 07	Y0PE0I03T
					RD	G400H	189	1992 Jun 07	Y0PE0I04T
B2 2201+31A	2201+315	02UD	22 03 15.02	31 45 37.7	BL	G130H	1390	1991 Sep 07	Y0PE0J02T
					BL	G130H	1400	1991 Sep 07	Y0PE0J03T
					BL	G190H	1104	1991 Sep 07	Y0PE0J04T
					RD	G270H	222	1991 Sep 06	Y0PE0K02T
					RD	G400H	132	1991 Sep 06	Y0PE0K03T
PKS 2216−03		02O6	22 18 52.08	−03 35 37.4	RD	G190H	666	1991 Sep 06	Y0PE0L02T[a]
					RD	G270H	486	1991 Sep 06	Y0PE0L03T[a]
					RD	G400H	294	1991 Sep 06	Y0PE0L04T[a]
					RD	G190H	666	1992 Aug 27	Y1170202T[a]
					RD	G270H	486	1992 Aug 28	Y1170203T[a]
					RD	G400H	294	1992 Aug 28	Y1170204T[a]
					RD	G190H	666	1993 Oct 03	Y1EM0102P
					RD	G270H	486	1993 Oct 03	Y1EM0103P
					RD	G400H	294	1993 Oct 03	Y1EM0104P
3C 446	2223−052	02O6	22 25 47.31	−04 57 01.4	RD	G270H	966	1991 Sep 11	Y0PE0M02T
					RD	G270H	960	1991 Sep 11	Y0PE0M03T
					RD	G400H	147	1991 Sep 11	Y0PE0M04T
CTA 102	2230+114	02CV	22 32 36.45	11 43 50.7	RD	G270H	954	1991 Sep 12	Y0PE0N02T
					RD	G400H	648	1991 Sep 12	Y0PE0N03T
3C 454.3	2251+158	00GO	22 53 57.77	16 08 53.3	RD	G190H	504	1991 Sep 11	Y0PE0O02T
					RD	G270H	954	1991 Sep 12	Y0PE0O03T
					RD	G400H	648	1991 Sep 12	Y0PE0O04T
PKS 2251+11		00JD	22 54 10.44	11 36 38.9	BL	G130H	1980	1991 Sep 06	Y0PE0P02T
					BL	G190H	732	1991 Sep 07	Y0PE0P03T
					RD	G270H	162	1991 Sep 06	Y0PE0Q02T
					RD	G400H	141	1991 Sep 06	Y0PE0Q03T

[a] FOS Binary Acquisition failed.

tron image is stepped in 20 0.25-diode intervals so that each part of the spectrum is sampled four times by each of five diodes, resulting in an image of 516 × 4 = 2064 pixels. Dispersions for the above grating setups are 0.25, 0.36, 0.51, and 0.75 Å/pixel. The 4″.3 × 4″.3 aperture was used for maximum throughput. In the direction perpendicular to the dispersion this aperture is effectively limited to 1″.4 by the length of the Digicon diodes, giving an effective aperture throughput of about 0.5–0.7 from 1300 to 4000 Å (because of *HST*'s spherical aberration). The targets were centered in the aperture using a Binary Acquisition, and the integrations made in the Accum mode (Ford & Hartig 1990). Centering and tracking is generally accurate to ∼0″.1, so spectral resolution is limited by the spectrograph itself, by the point-spread function of *HST*, and by GIM (see § 4.1). The effective resolution for a point source is 1.5 diodes FWHM—or 6 pixels (i.e., ∼350 km s^{-1}).

The wavelength scale, resolution, and the photometric accuracy of the spectra are affected by geomagnetic image motion (GIM, Koratkar 1994). This image motion is caused by a partial breakdown of the Digicons' magnetic shielding, so that peak-to-peak image shifts of up to 70 μm occur as the spacecraft orbits, as a result of the changing angle between the Earth's magnetic field and that of the Digicon tube. Fortunately, compensating shifts can be applied to the wavelength scale because data are read out at intervals that are short compared with the 90 minute orbit—2 and 4 minutes for the Red and Blue Digicons respectively. The effect is about three times smaller for the Blue tube than for the Red, and is unimportant for our Blue side spectra.

The exposure times were estimated to give a signal-to-noise ratio of at least 21 per resolution element in the continuum, in the region of important emission lines (Lyα, C IV λ1549, C III] λ1909 and Mg II λ2798). These estimates were based on a composite quasar spectrum derived from *IUE* and McDonald Observatory spectrophotometry of several radio-loud quasars. Figure 1 shows the expected count rate per diode (4 pixels) for

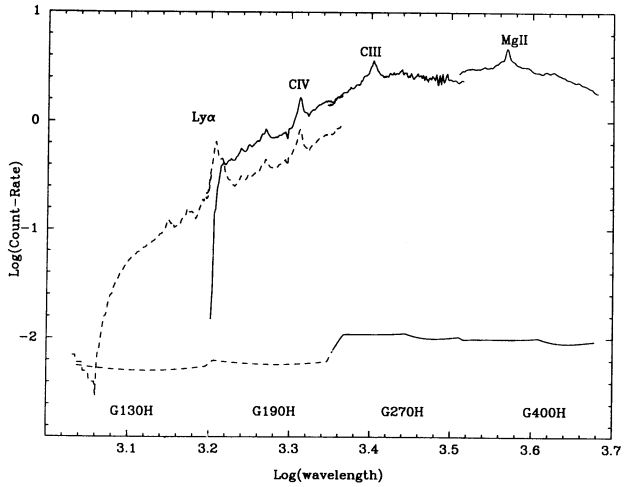

FIG. 1.—Example of the predicted count rates (counts s^{-1}) for a bright ($V \sim 15.8$), low-redshift ($z = 0.323$) quasar, PKS 2251+11. Coordinates are logarithmic to enable sensible scaling of the full wavelength range and the (modeled) detector background count rate. Filled and dashed lines are for the red and blue Digicon detectors. Note that for observations (of Lyα) near 1608 Å, the blue Digicon has significant sensitivity but the red does not.

The prediction is based on a composite spectrum formed from *IUE* and McDonald Observatory data, corrected for appropriate Galactic reddening, *V*-band magnitude, and redshift, which is then converted to count rate using FOS Handbook information on telescope and spectrograph throughput (for the 4.″3 aperture), and detector response.

a Cycle 1 target, as well as the expected count rates from detector background. We used the Blue Digicon rather than the Red for G190H if an important emission line fell between about 1550 and 1700 Å, because the response of the Red Digicon declines rapidly there. For Cycle 2, we used G400H only when important emission lines fell close to the atmospheric cutoff and so could not be observed accurately from the ground.

We are monitoring the photometric variability of our sample quasars at McDonald Observatory, with additional photometry from Wise Observatory, Tel Aviv University, and CTIO, a program that gives us information on changes in optical flux density for improved estimates of *HST* exposure times (and for more astronomical reasons).

4. REDUCTIONS

Appropriate flat-field– and GIM-corrected calibrated data became available through STScI's standard pipeline processing in 1992 May. Calibration was by the standard CALFOS "task" in the IRAF/STSDAS package. This task corrects the raw counts to flux density. It takes into account diodes that have been disabled at the spacecraft, corrects for the GIM wavelength shifts, subtracts a default instrumental background, divides by normalized flat fields derived from observations of white dwarf stars obtained closest in time to the quasar observations, and computes a wavelength scale accurate to about 0.1 diodes. The instrumental count rate is then corrected to flux density units. Finally, spectra from different grating settings are combined and corrected for Galactic extinction. Details are given below.

4.1. *Geomagnetically Induced Image Motion (GIM)*

For a single observation composed of several 2 or 4 minute readouts, the pipeline process shifts each readout (in the dispersion direction only), by an amount based on model calculations of the Earth's magnetic field. The shifts within a 2 or 4 minute integration cannot be corrected but our resolution (6 pixel FWHM) is degraded overall by less than 5% (Junkkarinen et al. 1992). The GIM also degrades the photometric accuracy (§ 4.5).

4.2. *Background*

Exceeding the natural diffuse Galactic background, zodiacal light, airglow, and scattered light internal to the FOS, is a burst-noise background induced by cosmic rays in the detector faceplate (Kinney 1992; see also Ford & Hartig 1990; Lyons et al. 1992a, b). Electronic dark count rate is negligible. A default background is subtracted, taking into account the geomagnetic position of the telescope at the time of observation. This is typically a few percent of our signal, except for 3C 216, for which the background was almost comparable to the signal. It is now suspected that a default background 30% larger is more appropriate (Rosa 1993), but the present reductions use the earlier estimate.

Scattered light, probably from the grating, can be a significant contaminant for objects with very red spectral energy distributions (Kinney & Bohlin 1993; Rosa 1993; Ayres 1993). A check on the background arising from scattered light within the spectrograph is given by observing the signal in a region of no sensitivity to the dispersed light (because of optical cutoffs). Such a region occurs at the short wavelength end of the G190H red spectrum, between pixels 2040 and 2059 (1582–1610 Å) (Kinney & Bohlin 1993), but we detect no significant signal here for individual objects. There is a small, significant signal when summed over many quasar spectra, but it amounts to less than a few percent of the smallest astronomical signal in this grating setting, so we have ignored it.

4.3. *Flat-Field Correction*

The diode-to-diode sensitivity variations of the Digicons are determined from observations of spectra of bright stars with smooth continua, usually white dwarfs (Anderson 1992). The flat fields seem to be time variable, especially for the Red Digicon between 1800 and 2100 Å where there are large spikes and dips; they are also dependent on the aperture selected, and position of the spectrum on the diodes (Jannuzi & Hartig 1994; Keyes 1994). We have used the flat-field calibration files determined from the calibration observation closest in time to that of our individual targets. Our data were reprocessed after the correction of the software error announced 1993 February 15 (Keyes, STScI notice). Fortunately both our quasar observations and the flat-field observations used the same 4.″3 aperture. We examined our final spectra in the regions of large spikes or dips in the flat fields, and found no evidence of spurious features.

4.4. *Wavelength Calibration*

We used the cubic polynomial dispersion relation provided in the FOS "pipeline." This was determined from an internal calibration lamp, and agrees with the external scale determined from the emission line star AU Mic, to ± 0.1 diodes (Kriss, Blair, & Davidsen 1992). The internal accuracy of wavelength calibration, after correction for GIM, is thought to be at the level of ~ 0.25 diode, or roughly 50 km s^{-1}, and the external accuracy ~ 0.4 diodes (Bohlin & Cox 1992).

TABLE 2

BASIC DATA AND STRONG LINE PARAMETERS[a]

Name		Lyα		C IV λ1549[b]		C III] λ1909 + Si III] λ1892		Mg II λ2798	
	z	Flux		Flux		Flux		Flux	
	logR	EW		EW		EW		EW	
	V	FW25M		FW25M					
	A_B	FW50M		FW50M		FW50M		FW50M	
	logLe	FW80M		FW80M					
	α_{uv}	Asym		Asym					
		Abs		Abs					
PKS 0112−01	1.365	6.8	g(7.1)	3.6	a	2.7	b	...	
	1.0	39	(40)	24		25		...	
	17.4	6503	cg	7995	b				
	0.20	3781	cg	5189	b	7063	c	...	
	27.0	2424	bg	2783	c				
	1.42	+0.01	cg	−0.06	c				
		1		2					
3C 47.0	0.425	29.6	g(32.2)	23.6	g(24.2)	6.3	a	...	
	−1.0	196	(213)	210	(215)	72		...	
	18.10	6520	bg	9555	bg				
	0.17	2713	bg	4273	bg	5324	b	...	
	26.8	...		1870	cg				
	0.76	...		−0.13	dg				
		3		2					
PKS 0403−13	0.571	30.8	a	25.4	a	4.4	a	5.0	a
	0.7	124		138		29		43	
	17.09	4806	a	5709	b				
	0.10	2740	a	3366	a	3317	b	3715	b
	26.9	1179	a	1533	a				
	1.05	+0.28	a	+0.26	a				
		3		3		a			
3C 175	0.768	109	g(113)	34.2	a	11.1	b	...	
	−1.5	165	(170)	58		25		...	
	16.60	14251	cg	15289	c				
	0.74	5734	ag	7161	b	8400	c	...	
	27.5	2106	dg	2168	c				
	0.85	−0.27	dg	−0.16	c				
		3		1					
3C 186	1.063	16.3	b	8.6	g(9.4)	2.23	b	...	
	<−1.4	117		76	(83)	24.4		...	
	17.60	10165	a	11089	cg				
	0.17	4005	b	5012	dg	5731	c	...	
	27.4	1164	d	...					
	0.95	−0.02	d	...					
		3		2					
3C 207	0.684	10.2	g(13.3)	11.1	g(12.4)	1.79	b	2.0	b
	−0.5	106	(138)	114	(127)	20		27	
	18.15	5112	cg	6760	cg				
	0.21	3218	dg	3803	dg	3463	b	3149	b
	27.5	...		...					
	1.83	...		...					
		3		3					
PKS 0859−14	1.327	26.4	a	...		...		...	
	0.81	80		...		...		...	
	16.59	6838	c	...					
	0.08	3938	a	...		...		...	
	27.5	1855	b	...					
	...	+0.05	b	...					
		0		...					

TABLE 2—*Continued*

Name	z logR V A_B logLe α_{uv}	Lyα Flux EW FW25M FW50M FW80M Asym Abs		C IV λ1549[b] Flux EW FW25M FW50M FW80M Asym Abs		C III] λ1909 + Si III] λ1892 Flux EW FW50M		Mg II λ2798 Flux EW FW50M	
3C 215	0.411	19.3	a	17.5	b	2.41	b	3.2	b
	−1.4	207		254		45		72	
	18.27	7048	a	9545	b				
	0.10	3975	a	5601	a	3385	b	6440	b
	26.6	1453	a	1643	a				
	0.64	+0.09	a	+0.09	a				
		2		0					
3C 216.0	0.670	...		...		...		...	
	−0.1	...		...		...		...	
	18.10	...		...					
	0.04	...		...		...		...	
	27.4	...		...					
	2.00	...		...					
		1		...					
B2 0923+39	0.699	69	g(73)	38.8	a	5.4	a	...	
	1.2	115	(121)	78		14.9		...	
	17.86	9292	ag	9870	b				
	0.02	4409	ag	4701	a	4861	b	...	
	27.0	2205	bg	2255	a				
	0.65	+0.17	ag	+0.24	a				
		3		0					
4C 55.17	0.901	5.42	a	3.58	a	...		...	
	0.32	49.1		38.2		...		...	
	18.1	4108	c	10503	b				
	0.00	1808	b	2944	c	...		...	
	27.5	787	b	1248	b				
	...	+0.41	c	+1.24	b				
		1		1					
PKS 1103−006	0.426	41.3	a	22.3	a	11.1	b	...	
	−0.1	122		63		37		...	
	16.46	8103	b	8690	b				
	0.12	4071	b	4176	b	7790	b	...	
	26.68	1943	b	1453	b				
	1.50	−0.15	b	−0.17	b				
		0		0					
3C 254	0.734	31.5	g(33)	19.5	b	2.8	b	...	
	−1.8	304	(320)	225		39		...	
	17.98	6619	bg	13172	a				
	0.08	2446	cg	5115	a	2969	c	...	
	27.5	...		1856	b				
	0.75	...		+0.19	a				
		3		3					
PKS 1127−14	1.187	13.3	b	...		...		...	
	1.7	56		...		...		...	
	16.90	8062	b	...					
	0.09	5198	c	...		...		...	
	26.8	2429	d	...					
	1.55	−0.07	d	...					
		3		...					

TABLE 2—*Continued*

Name	z logR V A_B logLe α_{uv}	Lyα Flux EW FW25M FW50M FW80M Asym Abs		C IV λ1549[b] Flux EW FW25M FW50M FW80M Asym Abs		C III] λ1909 + Si III] λ1892 Flux EW FW50M		Mg II λ2798 Flux EW FW50M	
3C 263	0.652	91.6	a	52.2	a	11.9	b	11.5	b
	−1.1	114		86		25.3		34	
	16.32	5571	a	6261	a				
	0.01	2742	a	3362	a	4567	c	4849	c
	27.5	1280	a	1622	a				
	0.77	0.00	a	0.00	a				
		1		1					
3C 277.1	0.320	...		21.8	g(22.5)	3.5	b	4.6	b
	−1.7	...		139	(143)	29		55	
	17.93	...		6007	cg				
	0.00	...		2719	cg	1922	c	3091	b
	26.8	...		1219	dg				
	0.70	...		+0.10	dg				
		...		3					
3C 279	0.538	5.11	b	5.42	a	1.17	b	2.1	c
	1.1	29		28.5		6.1		11	
	17.75	5048	c	12187	b				
	0.06	2385	b	5502	b	2769	c	4037	c
	27.0	1295	b	1715	c				
	2.07	+0.15	b	+0.64	b				
		0		0					
3C 288.1	0.961	8.2	g(8.8)	5.2	g(5.6)	...		...	
	−2.2	56	(60)	46	(50)	...		...	
	18.12	9472	dg	10815	d				
	0.01	3916	dg	5707	d	...		...	
	27.5	...							
	1.00	...							
		3		3					
PKS 1354+19	0.720	69.1	a	37.2	a	9.3	a	...	
	0.37	183		108		32		...	
	16.03	4222	a	6557	a				
	0.06	1909	a	2860	a	4134	b	...	
	27.1	917	a	1308	a				
	1.25	+0.03	a	0.00	a				
		1		0					
3C 323.1	0.264	176	g(187)	102	b	16.5	b	25	b
	−1.3	226	(241)	175		37		74	
	16.69	7475	cg	10606	a				
	0.14	3245	cg	4796	a	3616	b	5315	b
	26.5	1566	dg	1976	b				
	0.80	−0.01	dg	0.00	a				
		3		2					
B2 1555+33	0.942	6.25	a	5.08	a	...		...	
	0.0	122		121		...		...	
	18.3	7418	a	8804	a				
	0.08	2962	a	3838	b	...		...	
	26.5	1068	a	1390	a				
	...	+0.34	a	+0.25	a				
		1		2					

TABLE 2—*Continued*

Name	z logR V A_B logLe α_{uv}	Lyα Flux EW FW25M FW50M FW80M Asym Abs		C IV λ1549[b] Flux EW FW25M FW50M FW80M Asym Abs		C III] λ1909 + Si III] λ1892 Flux EW FW50M		Mg II λ2798 Flux EW FW50M	
DA 406	1.401	12.5	g(13.0)	7.39	g(7.45)	0.86	b	...	
	1.4	70	(73)	47.9	(48.3)	7.5		...	
	17.5	6160	cg	9678	cg				
	0.01	2575	cg	4774	cg	5575	d	...	
	27.0	...		2566	dg				
	0.75	...		+0.37	dg				
		3		1					
3C 334	0.555	68.5	a	44.3	a	11.0	b	12.8	b
	−0.7	121		99		31.6		56	
	16.41	10476	b	11983	b				
	0.14	5218	b	5063	a	7468	c	5224	c
	27.0	1499	d	1933	b				
	0.85	−0.16	c	−0.07	b				
		2		2					
OS 562	0.750	34.8	a	17.1	a	4.7	b	...	
	0.6	90		54.8		20		...	
	17.0	5655	a	7869	a				
	0.00	2762	a	3671	b	5013	c	...	
	27.4	1164	a	1655	b				
	0.92	−0.03	a	+0.16	b				
		0		1					
3C 345	0.594	35	b	30.4	a	6.5	b	6.7	b
	1.5	97		87		19.6		24	
	15.96	7625	b	8922	b				
	0.00	3803	b	4829	a	4098	c	4196	b
	26.6	1798	b	2100	a				
	1.58	+0.18	b	+0.22	a				
		3		1					
B2 2201+31A	0.297	254	b	147	a	62	b	45	b
	0.2	72		50.4		28		35	
	15.58	11938	b	11827	a				
	0.48	4394	a	5281	a	7184	b	4394	b
	26.6	2076	a	2466	a				
	1.00	−0.01	b	+0.07	a				
		1		1					
PKS 2216−038	0.901	30.0	a	18.0	a	4.6	b	...	
	1.1	110		68		19		...	
	16.38	7006	a	10321	a				
	0.20	2979	a	3714	b	6012	c	...	
	26.7	912	a	1366	a				
	...	+0.02	a	+0.19	b				
		1		0					
3C 446	1.404	6.86	a	5.1	b	0.92	c	...	
	1.5	109		75		15		...	
	18.39	5006	a	7581	b				
	0.20	2510	a	3449	b	4418	d	...	
	27.2	1125	a	1496	b				
	1.83	−0.06	a	+0.10	b				
		0		0					

TABLE 2—*Continued*

Name	z logR V A_B logLe α_{uv}	Lyα Flux EW FW25M FW50M FW80M Asym Abs		C IV λ1549[b] Flux EW FW25M FW50M FW80M Asym Abs		C III] λ1909 + Si III] λ1892 Flux EW FW50M		Mg II λ2798 Flux EW FW50M	
CTA 102	1.037	26.7	a	13.2	a	3.6	b	...	
	1.4	79		45		16		...	
	17.33	5563	b	6632	b				
	0.17	3083	a	3340	a	3903	b	...	
	26.9	1593	a	1661	a				
	0.88	+0.09	b	+0.13	b				
		1		1					
3C 454.3	0.859	26.7	a	14.4	b	6.2	b	...	
	1.2	74		41		20		...	
	16.10	4937	a	5254	a				
	0.26	2804	a	3145	a	5175	b	...	
	27.4	1364	a	1496	b				
	1.52	−0.04	a	0.00	a				
		0		2					
PKS 2251+11	0.323	95	g(105)	63	g(69)	22	b	19	b
	−1.5	136	(149)	117	(128)	49		38	
	15.82	5692	cg	7567	cg				
	0.15	2930	dg	3758	cg	5423	b	4598	c
	26.5	...		...					
	1.10	...		...					
		3		3					

[a] Entries of second column: z, redshift; log R, radio core dominance parameter; V, V magnitude; A_B, Galactic extinction in B band; log L_e, radio lobe luminosity; α_{uv}, UV spectral index ($F_\nu \sim \nu^{-\alpha_{UV}}$).

Line parameters: flux, observed frame integrated flux (10^{-14} ergs s^{-1} cm^{-1}); EW, rest frame equivalent width (Å); FW25M, full width ($c\,\Delta\lambda/\lambda$) at 25% of line peak (km s^{-1}). Asym, asymmetry parameter at 25% of line peak (0, a symmetric line; positive, strong long-wavelength wing). Abs, a flag indicating the strength of associated absorption (0, no absorption seen; 3, strong absorption). Line width and asymmetry measurements are of the observed profiles, with no attempt to correct for the fact that the line may be an atomic multiplet.

[b] C IV measurements include the ~λ1600 emission feature.

4.5. *Absolute Flux Density Scale*

The flux density calibration is important for our science because quasars are variable, and we need to combine these ultraviolet data with quasi-simultaneous ground-based data obtained at longer wavelengths.

The absolute flux density calibration was performed using the inverse sensitivity calibration files derived by STScI staff for each grating setting, using observations of the spectrophotometric standard stars, HZ 44, BD + 28°4211, and BD + 75°325 through the 4″.3 aperture, between 1991.4 and 1992.2 (Neill, Bohlin, & Hartig 1992; Taylor & Keyes 1993). The external flux density scale is thought to be accurate to from 10% to 5% over the range from 1300 to 3200 Å. The internal consistency of the scale is better than 5% (Bohlin & Neill 1992). With centering accuracy within ~0″.1, we expect uncertainties resulting from light losses to be negligible. However, the sensitivity for the blue G130H observations was decreasing by about 10% per year at all wavelengths, while the sensitivity of the red Digicon is constant within ~5%, except between 1800 and 2100 Å, where it was also declining by about 10% per year. In addition the PSF of *HST*'s aberrated image, and hence the aperture throughput, depends on *HST*'s focus, which changes (in a known way) with time (Lindler & Bohlin 1993). Pointing and tracking errors caused by GIM, solar array glitches, and perhaps an electronic drift of the spectrum in the direction perpendicular to dispersion, combined with the PSF and varying sensitivity (which may in fact be related to the focus changes and electronic drift), limit our present calibration accuracy to 5%–10% (Bohlin 1993; Koratkar & Taylor 1993; Evans 1993)—but with some hope of improved recalibration of these observations in the future.

As an internal check of the FOS flux calibration, we found that the flux densities in the regions of overlap between different gratings, 30–80 Å, agreed to within the rms uncertainties of ~8%. This is an upper limit as this comparison is least accurate at the ends of the arrays; the sensitivity is lower there for some configurations, and the electronic image is tilted and S-distorted at the diode array so the ends are most affected.

As a further check, we have compared our spectra with those observed by Bahcall et al. (1993) for four of our quasars in common. Bahcall et al. (1993) used the FOS with the 1″.0 diameter aperture. We find that the continuum flux ratios of Bahcall et al.'s spectra to ours are 0.99 for PKS 2251+113 (observations within 7 weeks), 1.08 for PKS 1354+195 (for which Bahcall et al.'s observations were made 14 months earlier and used the low-resolution G160L grating), 1.12 for 3C 263 (5 weeks apart), and 1.58 for 3C 454.3 (observations

separated by 2 months). The large ratio for 3C 454.3 reflects real continuum time variability; the emission-line strengths remained constant to within ~5%. Thus the spectra agree within the expected calibration uncertainty for the smaller aperture observations for which centering may contribute as much as a 20% error.

4.6. *Correction for Dead Diodes and Noise Spikes*

Except at the end of the spectrum, five diodes normally contribute to the flux density measurement at each wavelength. If a diode is known to be noisy or "dead" it can be disabled before data acquisition, and the count rates corrected on-line. In this case the flux density is nearly always recovered as it will generally be measured by four other diodes. Occasionally a single diode is dead and not recognized as such before the observation; conversely, a diode may be mistakenly flagged as dead. This affects 20 pixels, and their measured fluxes must be multiplied by 5/4 or, conversely, 4/5. A single, unrecognized, noisy diode would corrupt 20 pixels in the output spectrum. We noticed only two such problems that affected the line fitting. One was on the red side of Lyα of PKS 0112−01. The data were sufficiently noisy that the affected wavelength interval was excluded from subsequent analysis. The other was on the red wing of C IV for 3C 254; the affected region was also excluded. The interval very nearly coincided with the interval [1590 Å, 1620 Å] which was excluded from all the fits anyway (see § 5.1).

A few times in our whole data set, we noticed spikes affecting individual pixels, fortunately never near emission lines.

4.7. *Combining the Spectra, Galactic Extinction*

All the data for a given object were averaged in 3 pixel blocks. Each new combined point had wavelength and flux values from the $1/\sigma^2$ weighted average of the contributing data values. (The overlap regions used the 3 pixel intervals defined by the red or blue spectrum, depending on which half of the overlap the wavelength in question fell, but all data in any given interval were used.) The combined spectra were corrected for Galactic extinction using the empirical function derived by Cardelli, Clayton, & Mathis (1989, in IRAF) with $R = 3.2$ and the E_{B-V} values as given by Burstein & Heiles (1982).

The combined spectra are shown in Figure 2, separated into four groups (Figs. 2*a*–2*d*) according to ultraviolet spectral index, from $\alpha_{UV} = 0.5$ to 1.9, i.e., $F_\nu \propto \nu^{-\alpha_{UV}}$ or, in terms of F_λ used in Figure 2, $F_\lambda \propto \lambda^{\alpha_{UV}-2}$. The most prominent emission lines are indicated: Lyα, C IV λ1549, C III] λ1909, and Mg II λ2798. Note that all spectra are plotted on the same logarithmic flux density scale, so that line to continuum ratios can be directly compared. Further details are given in the figure caption.

5. MEASUREMENT OF CONTINUUM AND EMISSION LINES

Our aim here is to present first-order characteristics of the spectra—an ultraviolet spectral index, and line measurements: fluxes, equivalent widths, various line widths, and asymmetries for the prominent lines of Lyα, C IV λ1549, C III] λ1909, Mg II λ2798, and relative line strengths for these lines and weaker features. The largest uncertainties in determining the continuum shape arise from the lack of entirely line-free wavelength regions and, for the lower redshift quasars at lowest Galactic latitudes, uncertainties in the correction for Galactic extinction. For emission-line measurements, even for the least-blended line, C IV λ1549, the greatest uncertainties are usually in determining the true continuum level and in deblending the emission from weaker lines. For a few quasars, strong associated absorption in Lyα and C IV introduces significant uncertainty. In future papers, a combination of techniques, including spectral principal component analyses (e.g., Francis et al. 1992), will more fully explore the potential information in the complete data set, such as detailed differences between profiles of different lines.

The ultraviolet spectral indices $F_\nu \propto \nu^{-\alpha_{UV}}$ (Table 2, col. [2]) were determined from power laws fitted visually through the lowest continuum points near 1150, 1450, 1700, and 2050 Å, where available, taking into account the noise, and to a lesser extent, for a few quasars at the shorter wavelengths, uncertainties in Galactic extinction. For spectra with very broad lines, it is likely that none of these wavelength regions represents the true continuum; this was especially obvious near 1450 Å. Despite the uncertainties, this spectral index is well defined for most spectra.

Although we used Gaussian component fitting to deblend the regions of Lyα, C IV, and C III], profile measurements for these strong lines were made directly from the continuum- and blend-subtracted data to minimize their dependence on the appropriateness of the analytical fits. For the deblending, and for the flux measurements of weaker lines, we represented the profiles by two (or three) Gaussian components, with stronger constraints for weaker lines—the two- or three-Gaussian composite C IV profile was fitted to the weakest lines. Below we describe the procedure and present the results.

5.1. *Line Fitting and Deblending*

We subtracted from the total spectrum a continuum of the form

$$F_\lambda \propto \left(\frac{\lambda}{\lambda_0}\right)^{[a_0 + a_1(\lambda/\lambda_0)]},$$

where $\lambda_0 = 1549$ Å. Each profile was then represented by two (or three) Gaussian components, where the relative shifts from the nominal line center and the FWHM of each component were fixed at the same values for all lines. The parameters were determined by hand using C IV and Lyα with consideration for N V and the other lines in the wings of the stronger features. We then fitted the amplitudes only, for all components and for all lines, by a simultaneous linear least-squares method.

Next we reran the least squares fit to all lines, with the same relative velocity shifts and velocity widths for the components, but with the following constraints. For the strong lines, the two (or three) amplitudes were unconstrained. For N V λ1240 and C III] λ1909, either two amplitudes were unconstrained, or, when three components were used, the ratio of the amplitudes of the two broadest was fixed at the C IV value. For the remaining (weak) features (see Table 3) we fixed the relative amplitudes of all two or three Gaussian components at the values previously found for C IV.

Several details should be mentioned. First, in cases of atomic multiplets with significant member separation, each member of the multiplet included the two (or three) Gaussian components, with flux ratios among members determined by the ratios of atomic levels' statistical weights. Also the O I λ1303 triplet and the Si II λ1307 doublet were assumed to contribute equal flux to the blend. Similarly, the flux of the Si IV λ1397 doublet was set equal to that of the O IV] λ1402 multiplet. These weights are summarized in Table 4.

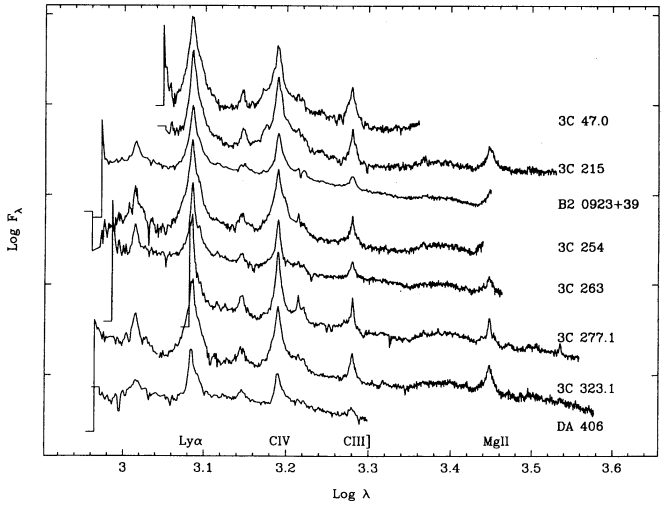

FIG. 2*a*

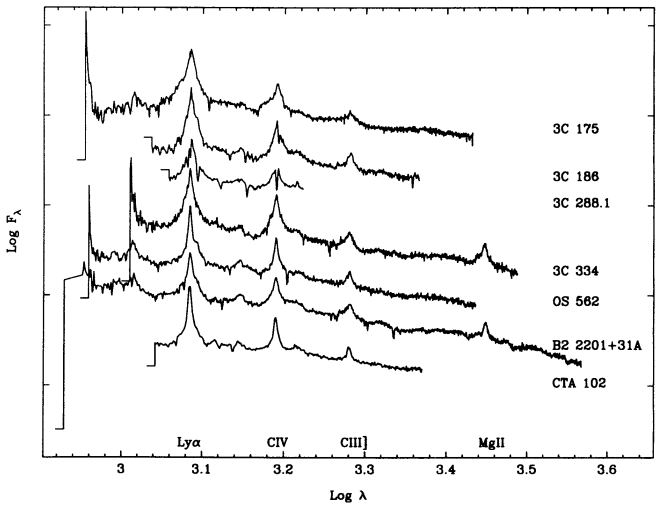

FIG. 2*b*

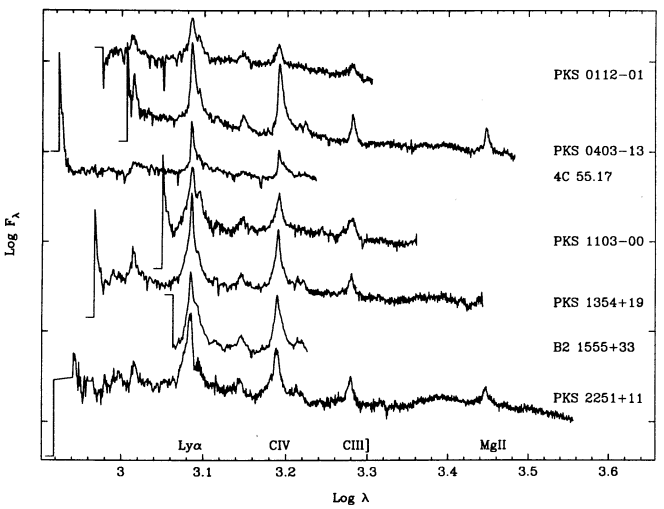

FIG. 2*c*

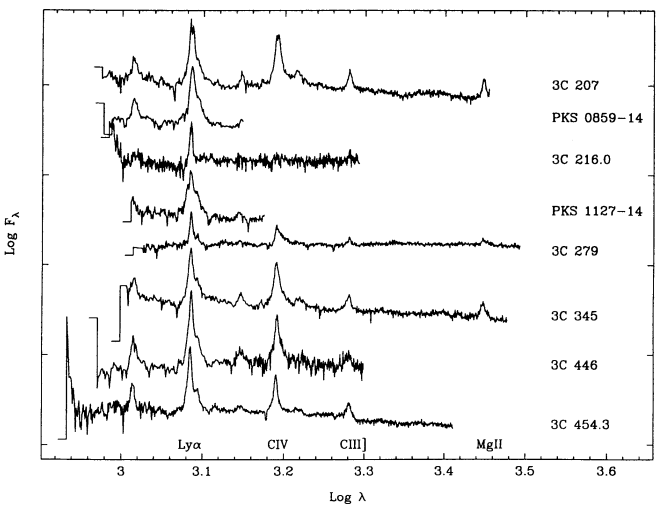

FIG. 2*d*

FIG. 2.—Spectra of radio-loud quasars observed with the Faint Object Spectrograph of the *Hubble Space Telescope*. Observed flux density (F_λ) is plotted vs. rest wavelength. All spectra are corrected for reddening within our Galaxy. They are shown in four panels, (*a*)–(*d*), according to ultraviolet spectral index, from flattest ($F_\nu \propto \nu^{-0.5}$) to steepest ($F_\nu \propto \nu^{-1.9}$). Within each panel the quasars are represented in order of right ascension; (*c*) and (*d*) include only the most variable, core-dominant quasars. The scales in log F_λ are the same in each panel, so that line-to-continuum ratios may be compared directly, but the scales are displaced for display purposes. The bars connected to the short-wavelength ends of the spectra represent observed flux densities of 10^{-15} ergs s^{-1} cm^{-2} Å^{-1}. For display purposes the data are shown binned by eight (original) pixels for the G130H data (the resolution in the original spectrum is about six original pixels), and approximately equivalent to the wavelength resolution for the G190H–G400H spectra. The most prominent emission lines are indicated: Lyα λ1216, C IV λ1549, C III] λ1909, and Mg II λ2798.

Second, in the region of 1600 Å, the effect of excess emission attributed to Fe II and possibly other species (Laor et al. 1994; Netzer & Wills 1983; Wills, Netzer, & Wills 1980) was reduced by removing the interval between 1580 and 1610 Å from the fit. Similarly, for the λ1909 feature, we removed the region beyond 1950 Å.

Third, there were several regions where the estimated continuum did not always match the data very well, so a local continuum was defined and the affected lines refitted. The Balmer continuum, Fe II, and possibly other blended emission form a quasi-continuum near C III] λ1909, and especially in the region of Mg II. Only integrated flux and FWHM (=FW50M) were measured for the Mg II and C III] λ1909 lines. Because of the uncertain continuum extrapolation and the generally poor signal-to-noise ratio at wavelengths below Lyα (see Fig. 2), here we have redefined a local continuum and fitted the C IV template by hand at the nominal wavelengths of C III λ977, N III] λ991, Lyβ, and O VI λ1034.

Lastly, we note that the linear least-squares algorithm included a loop that prevented negative values for line component fluxes. Although our procedure produced a satisfactory set of fitted values, in the presence of zero-valued components the fit is technically nonlinear. In these cases the uncertainties and the upper limits derived from the fit are still useful, although approximate. Anyway, uncertainties in the continuum level dominate.

5.2. *Line Measurements: Results*

Measurements of the Lyα, C IV, C III], and Mg II profiles are given in Table 2, and details of the profiles and fitted blends are

TABLE 3

LINE INTENSITIES RELATIVE TO C IV[a] FIT RESULTS[b]

Name	CIII] λ977 [g]	NIII] λ991 [g]	Lyβ λ1025.7 [g]	OVI λ1034 [g]	Lyα λ1216	NV λ1240	NV lb λ1240 [c]	SiII λ1263	λ1306 [d]	CII λ1335	λ1400 [e]	NIV] λ1486	HeII λ1640	OIII] λ1665	NIII] λ1750	SiII λ1814	AlIII λ1857	λ1908 [f]
PKS 0112−01	0.12 c	0.12 c	<0.18	0.80 b	2.09 a	0.92 a	>0.16	0.098 c	<0.092	0.067 c	0.37 a	<0.055	0.14 b	<0.1	0.099 b	<0.075	0.094 c	0.681 a
3C 47.0 [h,i]	...	...	...	...	1.24 [j] a	0.501 as	>0.033	<0.046	<0.016	<0.012	0.102 a	0.144 as	0.131 as	0.076 as	0.059 as	0.025 bs	<0.017 s	0.277 a
PKS 0403−13 [h,i]	...	...	...	0.28 [j] b	1.26 a	0.073 c	>0.041	0.038 b	0.074 a	0.017 b	0.118 a	<0.011	0.083 a	0.098 a	0.033 a	<0.017	<0.018	0.203 a
3C 175	...	...	...	0.32 b	3.15 a	<0.18	>0.032	0.039 as	0.153 as	0.157 as	0.175 as	0.064 as	0.073 as	<0.028 s	<0.011 s	0.017 cs	<0.027 s	0.305 a
3C 186 [h]	...	...	...	...	1.97 a	0.092 c	>0.056	0.165 a	0.111 a	0.046 b	0.146 a	0.044 b	0.216 a	0.051 c	0.026 c	<0.022	<0.035	0.26 b
3C 207	...	...	0.048 c	0.19 b	1.03 a	0.096 b	>0.027	0.049 b	0.0317 a	<0.007	0.100 a	0.039 a	0.183 a	0.082 a	0.044 [k] a	<0.019 [k]	<0.016 [k]	0.173 [k] a
PKS 0859−14 [l]	...	...	<0.044	0.18 b	1 a	0.176 a	>0.043	0.027 b	0.029 b	<0.021	0.11 [j] as	...	...	...	...	...	...	...
3C 215 [m]	...	...	...	...	1.18 a	0.2 b	>0.009	<0.025	0.0314 a	<0.008	0.111 a	0.094 [n] cs	0.13 [n] cs	0.053 [n] cs	0.0405 a	0.01 c	<0.0078	0.156 a
B2 0923+39 [h]	0.02 c	0.03 c	<0.04	0.38 a	1.69 a	<0.088	>0.027	0.084 a	0.078 a	0.029 a	0.133 a	<0.011	0.102 a	0.0742 a	0.014 [k] bs	<0.008 [k]	<0.013 [k]	0.144 [k] a
4C 55.17	...	...	<0.12	0.29 cs	1.64 a	<0.19	>0.009	0.086 c	0.13 b	<0.038	0.11 b	<0.034	0.197 as	0.225 [j] as	...	...	...	...
PKS 1103−006	...	...	...	...	1.93 [j] a	0.47 b	>0.21	0.17 b	0.133 a	<0.038	0.28 a	0.056 b	0.12 b	<0.072	0.106 a	<0.031	<0.049	0.543 a
3C 254 [h,i]	...	...	...	0.31 a	1.51 a	<0.14	>0.052	0.023 c	0.084 a	0.023 b	0.19 a	0.036 b	0.13 a	0.057 a	0.021 b	0.012 c	<0.029	0.151 a
PKS 1127−14 [l]	...	...	...	0.17 [j] cs	1 a	0.312 a	>0.077	0.102 a	0.047 b	0.019 c	0.124 a	...	...	...	...	...	...	...
3C 263 [h,i]	...	...	...	0.38 a	1.66 a	0.4 b	>0.061	<0.075	0.104 a	0.055 a	0.197 a	<0.023	0.095 a	0.066 a	0.015 [k] c	<0.026 [k]	<0.019 [k]	0.244 [k] a
3C 277.1	...	...	...	...	<2.8 [j]	<0.71 [j]	>0.024	<0.081	0.043 b	0.04 b	0.17 a	<0.02	0.172 a	0.062 a	0.021 bs	0.012 cs	0.037 as	0.167 a
3C 279 [h,i]	...	...	...	...	0.88 b	<0.27	>0.055	<0.097	0.088 bs	0.149 as	0.228 as	0.077 as	0.083 b	0.071 b	0.098 [k] as	<0.058 [k]	<0.053 [k]	0.219 [k] a
3C 288.1	...	...	...	...	1.81 as	0.49 bs	>0	<0.18	0.096 bs	0.078 bs	0.279 as	<0.085	0.296 [j] as	<0.077 [j]	...	...	...	...
PKS 1354+19 [h]	0.07 c	<0.08	<0.04	0.37 b	1.7 a	<0.1	>0.027	<0.022	0.076 as	0.016 cs	0.138 a	<0.018	0.090 a	0.079 a	<0.016	<0.025	0.019 c	0.237 a
3C 323.1	<0.02	<0.02	<0.04	0.42 a	1.73 a	<0.094	>0.012	<0.035	<0.029	<0.024	0.164 a	<0.015	0.118 a	0.077 a	0.015 b	0.013 b	<0.014	0.178 a
B2 1555+332 [h]	...	...	...	...	1.26 [j] a	0.19 b	>0.037	0.068 b	0.051 b	<0.015	0.153 a	0.025 b	0.147 [j] a	0.062 [j] a	...	...	...	...

TABLE 3—*Continued*

Name	C III [g] λ977	N III [g] λ991	Lyβ [g] λ1025.7	O VI [g] λ1034	Lyα λ1216	N V λ1240	N V *lb* [c] λ1240	Si II λ1263	λ1306 [d]	C II λ1335	λ1400 [e]	N IV] λ1486	He II λ1640	O III] λ1665	N III] λ1750	Si II λ1814	Al III λ1857	λ1908 [f]
DA 406 [h]	<0.04	0.09	0.16	0.16	1.84	<0.16	>0.028	0.123	0.069	0.089	0.273	<0.04	0.155	0.065	<0.043	<0.031	<0.035	0.14
		c	c	c	a			as	bs	bs	a		a	b				c
3C 334	...	...	...	...	1.57	<0.1	>0.003	0.094	0.15	0.069	0.141	<0.013	0.175	0.084	0.081	0.036	<0.028	0.272
					a			bs	as	as	a		a	as	as	bs		a
OS 562 [h]	0.15	<0.03	<0.10	0.45	1.95	0.19	>0.059	<0.037	0.041	0.054	0.296	<0.029	0.071	0.101	0.041	0.028	<0.043	0.29
	c			c	a	b			bs	bs	a		bs	as	bs	cs		b
3C 345	...	...	...	0.25 [j]	1.25	<0.16	>0.026	<0.081	0.097	0.086	0.188	0.061	0.097	0.117	0.057 [k]	<0.026 [k]	<0.041 [k]	0.2 [k]
				cs	a				as	as	a	bs	bs	as	bs			b
B2 2201+31A	0.17	0.18	<0.09	0.56	1.77	<0.12	>0.051	0.043	<0.025	0.047	0.265	<0.011	0.233	0.057	0.018	0.033	0.032	0.398
	c	c		b	a			cs		bs	a		as	as	bs	bs	bs	a
PKS 2216−03 [h]	0.10	<0.05	<0.08	0.27	1.7	0.38	>0.032	0.18	0.184	0.045	0.286	0.067	0.199	0.137	0.17	<0.04	0.072	0.28
	c			c	a	a		a	a	b	a	b	a	a	a		b	b
3C 446	0.048	0.021	<0.065	0.33	1.48	0.313	>0.035	0.05	0.079	0.068	0.16	<0.047	<0.058	<0.1	<0.053	<0.059	<0.065	<0.38
	c	c		b	a	as		bs	as	as	bs	s	s	s	s	s	s	s
CTA 102	...	...	...	...	2.15	0.206	>0.02	0.064	0.152	0.062	0.177	<0.021	0.177	0.0961	0.042 [k]	<0.021 [k]	<0.024 [k]	0.293 [k]
					a	a		b	a	b	a		a	a	b			a
3C 454.3	0.07	0.07	<0.11	0.45	1.82	0.25	>0.086	0.041	0.113	0.042	0.175	0.032	0.122	0.084	0.064	0.091	0.058	0.433
	c	c		b	a	b		b	a	b	a	b	a	a	as	as	bs	as
PKS 2251+11	...	...	...	0.31	1.77	0.24	>0.04	0.094	0.117	0.026	0.202	0.058	0.148	0.0487	0.047 [k]	0.065 [k]	0.027 [k]	0.399 [k]
				cs	a	c		c	a	c	a	b	as	a	s a	b	c	a

[a] Line intensities of PKS 0859−14 and PKS 1127−14 are relative to Lyα since C IV was not observed with *HST*. Uncertainty indicators a, b, c, and s are below each value (see text). The uncertainty indicator for C IV flux was "a" for all objects except 3C 288.1, which has extreme absorption in its profile, and 3C 215 (see notes l, m below). Note that the uncertainty indicators for the other lines do not include the uncertainty of the C IV flux.

[b] 3C 216.0 was not fitted with the standard technique.

[c] N V *lb* is a minimum flux measurement for N V λ1240. See text.

[d] λ1306 refers to the O I λ1303 triplet–Si II λ1307 doublet blend, set to have equal strengths.

[e] λ1400 refers to the Si IV λ1397 doublet–O IV] λ1402 multiplet blend, set to have equal strengths.

[f] λ1908 refers to the Si III] λ1892–C III] λ1909 blend. These two lines were fitted independently, but the total flux is given. In most of the fits λ1892 contributes 10% to 35% of the flux in the blend.

[g] C III λ977, N III λ991, Lyβ, and O VI λ1034 were refitted using a locally defined continuum.

[h] Central narrow component of Lyα was excluded from the fit.

[i] Central narrow component of C IV was excluded from the fit.

[j] Line is at edge of spectrum and therefore prone to extra uncertainties.

[k] N III] λ1750, Si II λ1814, Al III λ1857, Si III] λ1892, and C III] λ1909 features were refitted using a locally defined continuum.

[l] A template derived from Lyα was used for the weak features because C IV was not observed with *HST*.

[m] A template derived from Lyα was used for the weak features because the C IV profile was not well fitted with the three-Gaussian template. The complex line profile and a poorly defined continuum under Lyα make the fluxes of lines in the wings of strong features very uncertain, especially N V λ1240.

[n] The lines surrounding C IV were refitted by hand because of poor agreement ot the template with the spectrum, possibly due to unusually strong unidentified blended lines.

TABLE 4

WEIGHTS FOR COMPONENTS OF EMISSION FEATURES

λ_{eff} (Å)	Species	λ_{vac} (weight) ...				
1034	O VI	1031.93 (0.67)	1037.62 (0.33)			
1240	N V	1238.81 (0.67)	1242.80 (0.33)			
1263[a]	Si II	1260.42 (0.33)	1264.74 (0.60)	1265.00 (0.07)		
1306[b]	O I	1302.17 (0.56)	1304.87 (0.33)	1306.03 (0.11)		
	Si II	1304.37 (0.33)	1309.27 (0.67)			
1335	C II[c]	1334.53 (0.33)	1335.66 (0.07)	1335.71 (0.60)		
1400[b]	Si IV	1393.76 (0.67)	1402.77 (0.33)			
	O IV][c]	1397.21 (0.012)	1399.78 (0.22)	1401.16 (0.46)	1404.80 (0.09)	1407.39 (0.22)
1549[a]	C IV	1548.20 (0.67)	1550.77 (0.33)			
1664[a]	O III]	1660.80 (0.29)	1666.14 (0.71)			
1750	N III][c]	1748.65 (0.21)	1749.67 (0.48)	1752.16 (0.08)	1754.00 (0.23)	
1814	Si II	1808.01 (0.33)	1816.93 (0.60)	1817.45 (0.07)		
1860	Al III	1854.72 (0.67)	1862.79 (0.33)			

[a] These features are likely to be blended with Fe II.
[b] The two species were assumed to contribute equally.
[c] The values used were slightly different from those presented here.

shown in Figure 3. For all four lines we give integrated flux, equivalent width, and FW50M values. In addition, for the Lyα and C IV profiles we give measures of full width at 25% and 80% of the peak amplitude (FW25M and FW80M), and an asymmetry parameter

$$\text{Asym} \equiv \frac{\lambda_{25} - \lambda_{80}}{\text{FW50M}},$$

where λ_{25} and λ_{80} are the central wavelengths measured at the 25% and 80% levels. The Lyα and C IV lines also have an estimated index of associated absorption (0 = no absorption visible, 3 = strong).

As described above, the Lyα measurements exclude contributions from N V and weaker blends at longer wavelengths. The C IV measurements exclude contributions from N IV] λ1486, He II λ1640, and O III] λ1663, but, as there is no reliable way to separate the C IV long-wavelength wing from the excess emission sometimes seen between C IV and the He II–O III] blend, this is included in the C IV measurements. Fitted components of Si II λ1814 and Al III λ1857 were removed if they significantly affected the C III] λ1909 profile, but we could not distinguish the Si III λ1892 feature well enough to remove it.

Measurement uncertainties are denoted by a, b, or c, referring to ≤10%, 10%–20%, and 20%–33%, respectively. In addition, d refers to problems with profile shape measurements, such as where strong absorption required uncertain interpolation. In cases where the line peak was very uncertain because of apparent absorption, we have listed two flux (and EW) values. The first measurement of line strength is made by interpolating linearly across the absorption, and so is an estimate of a lower limit on the flux; the second (in parentheses) is derived from an estimate of the unabsorbed profile shape. Where widths and Asym depend on an estimate of the unabsorbed profile shape, we note this by a "g."

Table 3 shows the intensities of all lines, relative to C IV, determined from the C IV template fit as described in § 5.1. For Lyα, C IV, and the C III] λ1909–Si III λ1892 blend the fluxes of Table 2 are preferred, as the profiles of these stronger lines often deviate significantly from the three-Gaussian component template for C IV. The a, b, and c represent uncertainties as for Table 2. These do not include systematic uncertainties arising from absorption lines or continuum placement, which are often dominant for the weaker lines, and may correlate from line to line. The continuum placement is especially uncertain where weak lines occur in the wings of the strong lines, such as Si II λ1260 in the wing of the Lyα–N V λ1240 blend, or N IV] λ1486 in the wing of C IV λ1549. The "s" represents such an unquantifiable source of systematic error in particularly problematic cases. We have not included uncertainties resulting from unidentified weak blends. In particular, Fe II emission blends are expected to contribute significantly near 1260 Å and in the He II λ1640–O III] λ1663 region. Lyγ at 972 Å may contribute to C III λ977.

Because of the importance of N V in studies of the BLR abundances (Hamann & Ferland 1993) and the sensitivity of the measured N V flux to the chosen Gaussian parameters for Lyα, we estimated lower limits to its flux by integrating the spectrum above an interpolated smooth wing of Lyα, in the region of $\lambda_{\text{rest}} \sim 1240$ Å. These values are shown in Table 3, in the column marked "N V *lb*." If there is no significant bump, we have given 0.0 as the lower limit.

6. DISCUSSION

Although the 31 ultraviolet spectra presented here will be discussed in much more detail when we present the combined ultraviolet, optical, and infrared spectroscopy, we are able to make some unique observations here because this paper adds very significantly to the few good signal-to-noise ratio and good resolution (~350 km s^{-1}) ultraviolet spectra that are available for low- and intermediate-redshift quasars.

The strengths of lines below Lyα are difficult to measure in quasars observed from the ground because, at high redshifts, this region of the spectrum is confused by Lyα forest absorption by intergalactic clouds. The emission lines predicted to be strongest here are Lyβ at 1025 Å, C III λ977, O VI λλ1032, 1038, and N III λλ990, 992, but there are a number of other lines that may contribute—O I at 972, 974, 988, and 1026 Å, Fe II emission, and perhaps Si II. The O VI λ1034/Lyα line ratio is a good measure of the ionization parameter. The C III λ977 line is very important in determining the density of the BLR gas. In particular, it is predicted to be strong at very high densities ($\geq 10^{11}$ cm^{-3}) when the other important cooling agents (C IV λ1549,

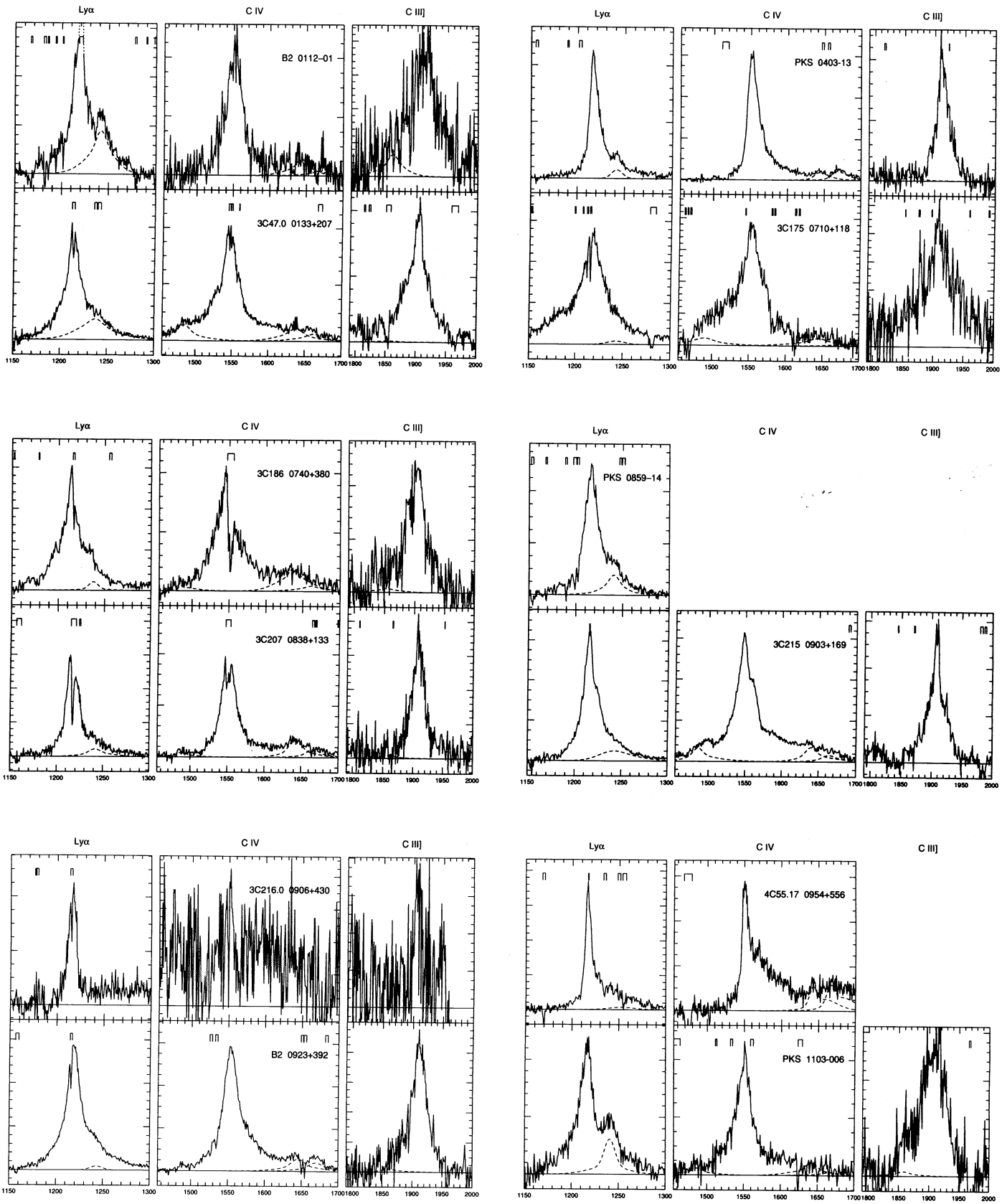

FIG. 3.—Details of the continuum-subtracted profiles for strong emission lines. Dashed profiles are fits to weaker blends that have been subtracted from the data before measuring the strong emission line parameters (see § 5.1). The ordinate is F_λ. Rest wavelengths are shown, and the abscissa scale of the plots is such that profiles can be compared directly in velocity. Galactic, intervening intergalactic, and associated absorption systems are indicated.

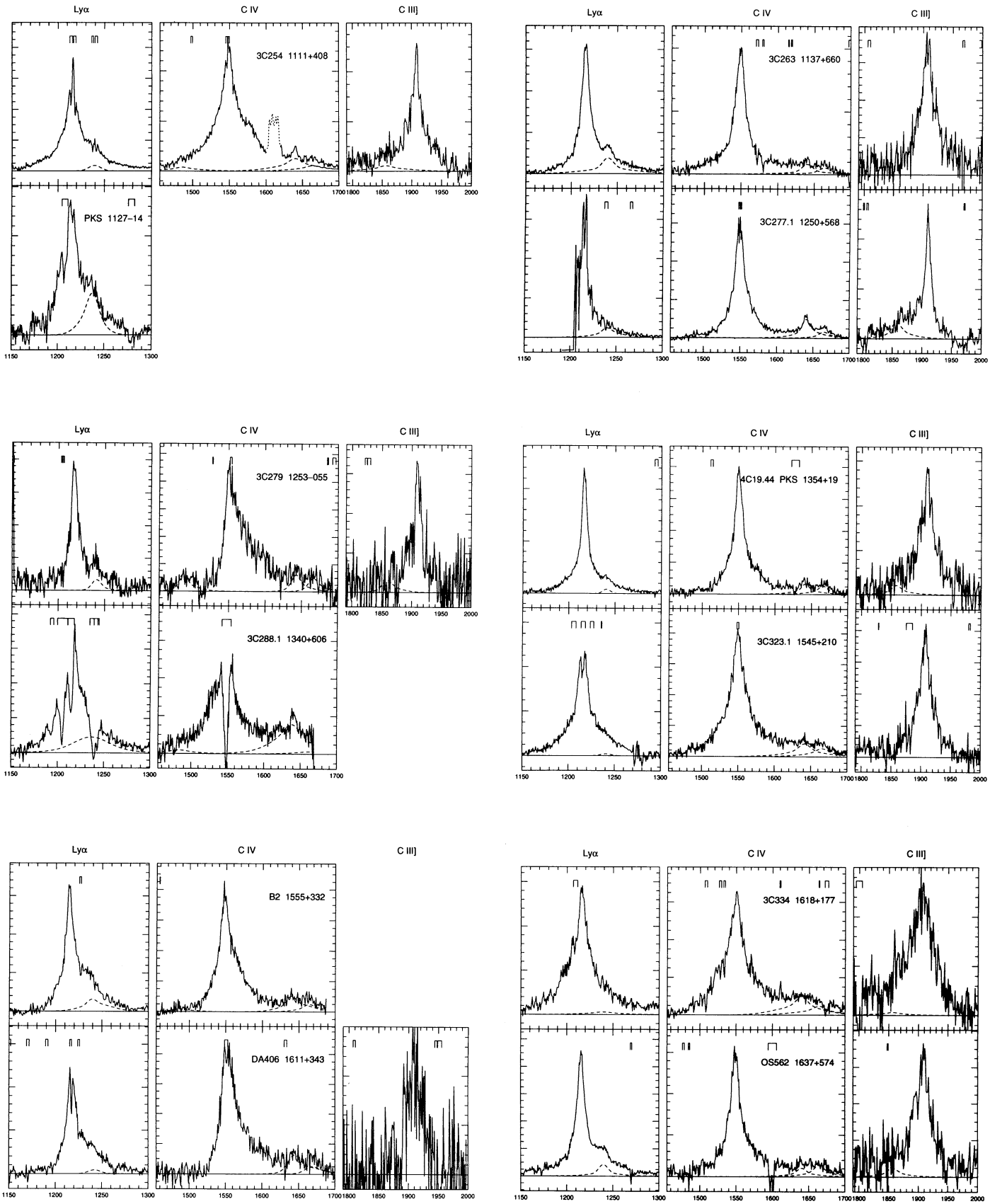

FIG. 3.—*Continued*

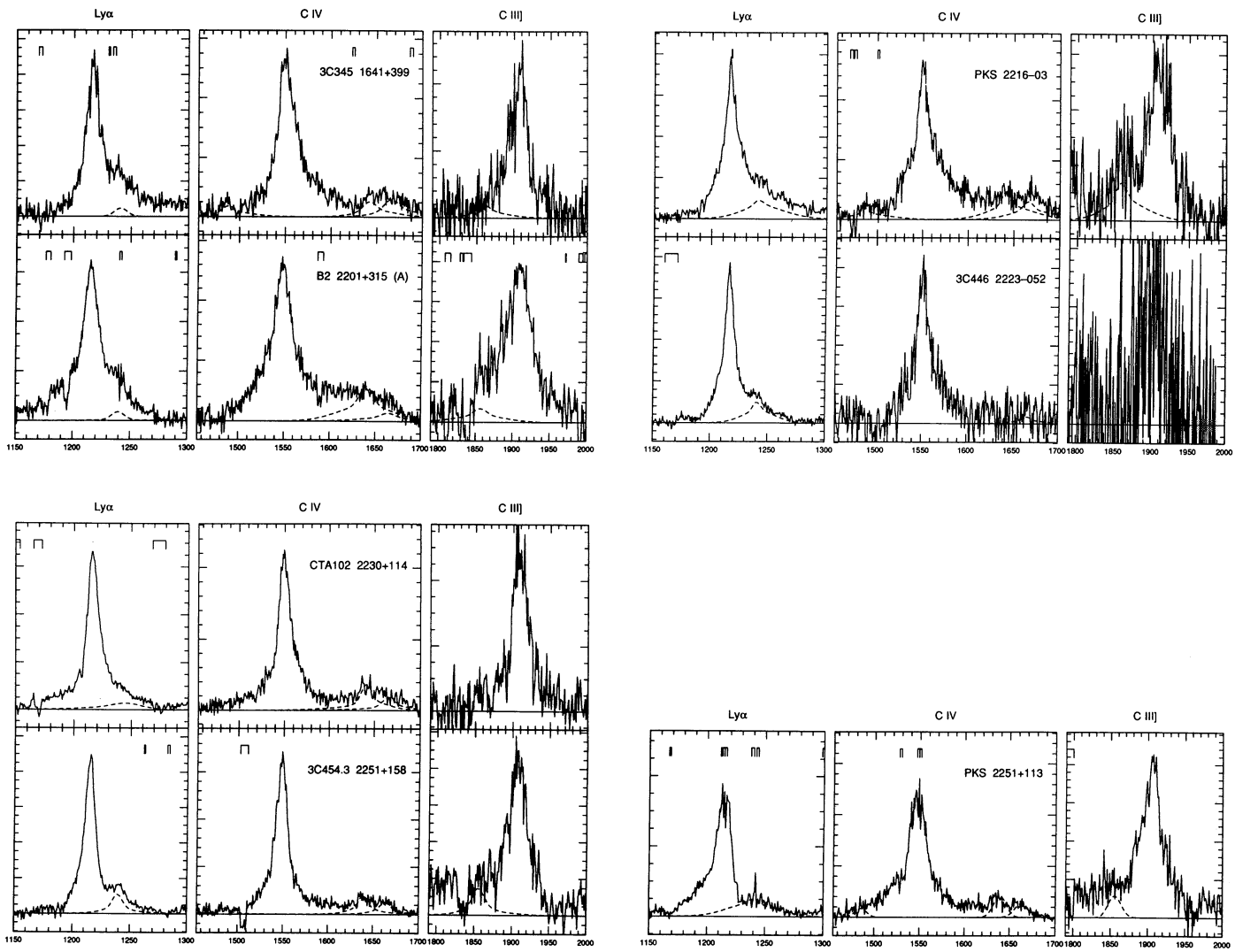

FIG. 3.—*Continued*

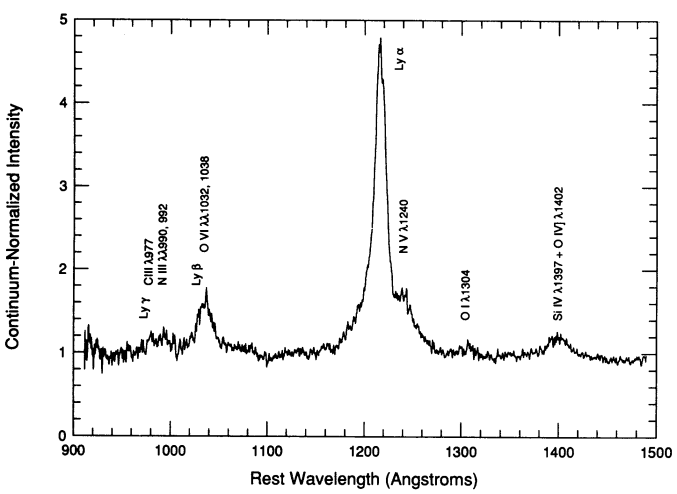

FIG. 4.—Spectral region from rest wavelengths 912 to 1500 Å derived from a composite of the spectra of B2 2201+31A, PKS 2251+11, OS 562, and 3C 454.3. It shows the expected wavelengths of weaker features below 1216Å: Lyγ, C III λ977, N III λλ990, 992, Lyβ, and O VI λλ1032, 1038.

N V λ1240 emission, etc.) are collisionally suppressed (Rees, Netzer, & Ferland 1989).

We have co-added four of the best spectra that extend to about 912 Å rest wavelength, and the result is shown in Figure 4, where the rest wavelength scale is defined by the peak of the C IV λ1549 line, assumed to be at 1549.0 Å rest wavelength. The strong feature measured at 1035.6 Å is clearly dominated by O VI λ1034, while Lyβ is a very minor contributor with an upper limit of less than 15% of the λ1035 feature in all except the noisiest spectra. The high-ionization O VI line in the composite, or in individual quasar spectra, does not appear to be strongly blueshifted as is observed for some QSOs in some other high-ionization lines (e.g., Espey et al. 1989). The next strongest feature peaks near 990 Å, suggesting that N III λ991 dominates at this wavelength. In the composite, this feature is asymmetric with a stronger short-wavelength wing. This is probably C III λ977 emission which, in some spectra, can be stronger than N III λ991. Typical line intensities, normalized to 100 for Lyα, are C III λ977, N III λ991, O VI λ1034, N V λ1240, C IV λ1549, C III] λ1909 = 5, 4, 23, 14, 56, 15, although the intrinsic dispersion is large. There is often clear, excess emission near 1080 Å and between 1100 Å and Lyα (Fig. 4).

Our measurements of the O VI λ1034/Lyα ratio cover the range 0.1–0.4, with a mean of $\sim$0.21. The ratio (O VI λ1034 + Lyβ)/(Lyα + N V λ1240) measured in lower resolution *IUE* spectra of similar low-redshift quasars by Kinney et al. (1985, 1987) is in good agreement with our measurements, including agreement within $\pm$0.02 for the ratios of the three objects in common (see also Laor et al. 1994). The only careful measurements for high-redshift quasars that we could find, removing obvious Lyα forest absorption, were by Wilkes (1984): 0.18 and 0.09. We have attempted the same measurements using the high-redshift, high-resolution data of Sargent, Steidel, & Boksenberg (1989) and Sargent, Boksenberg, & Steidel (1988) and find values consistent, on average, with all the above values: there is no evidence yet for a difference between high- and low-redshift quasars. Our new data for the O VI λ1034/Lyα line ratio confirms the suggestion (e.g., Ferland & Persson 1989) that high-ionization material and a small BLR is required in order to explain the emission-line spectrum.

The C III λ977 line is very weak or undetectable in a wealth of *HST* archival spectra (e.g., Bahcall et al. 1993). Ours are perhaps better than previous data in this region (e.g., Laor et al. 1994, 1995). Still, we find it to be quite weak, with mean ratio C III λ977/Lyα $\sim$0.05, suggesting models with density $\lesssim 10^{10-11}$ cm^{-3} (Rees et al. 1989). Note that these densities are an average over the entire BLR, and the weak C III λ line intensity does not exclude a small region with a much higher density.

We have detected the N III λ991 line in a few objects, with up to $\sim$5% of the Lyα intensity. Given the intrinsic dispersion, this is consistent with results by Laor et al. (1994, 1995).

The continua and line profiles show some striking trends.

The spectra shown in Figures 2*a*–2*d* are ordered by continuum spectral index, α_{UV}. Plotted as log F_λ versus log λ, they appear increasingly flat; on a presentation more conventional for spectral energy distributions, they are increasingly steep: $F_\nu \propto \nu^{-\alpha_{UV}}$, with α_{UV} increasing from about 0.5 to 1.9. We note the striking but not surprising trend—the high α_{UV} spectra of Figures 2*c* and 2*d* are all of time-variable, core-dominant quasars (Fig. 5). Lobe-dominant sources are present only in Figures 2*a* and 2*b*. Although there are some core-dominant quasars in Figures 2*a* and 2*b* we note that these sources are either variable but not especially bright at the time of our observations or they are core-dominant but belong to the class of *steep radio spectrum* core-dominant sources. We also note a significant decrease in emission-line EW with increasing core dominance. This, and the steep ultraviolet spectrum, is at least partly the result of a significant contribution from a synchrotron component (Wills 1991; Wills et al. 1995).

We also note a tendency for the broad C IV λ1549 lines of core-dominant objects to show strong red wings; see, in particular, 3C 279 (see also Netzer et al. 1994) and 4C 55.17. None shows stronger blue wings. Lobe-dominant quasars show more symmetric profiles. These profiles contrast sharply with the strong blue wing asymmetry of radio-quiet QSOs (Fig. 6). There is almost no overlap in Asym (at 20% or 25% of peak line intensity) between core-dominant and radio-quiet QSOs, and the differences between core-dominant or all radio-loud quasars and radio-quiet QSOs are highly significant (using the Wilcoxon summed rank test). The "radio-quiet" sample used is described by Wills et al. 1993b; not all are confirmed radio-quiet, so the two with stronger red wings may later turn out to be radio-loud. This difference does not appear to depend on optical luminosity, as radio-quiet QSOs from the *HST* archives matched to the luminosity of our radio-loud sample show the same effect. Profile differences between the core- and lobe-dominant sources, or between lobe-dominant and radio-quiet QSOs, are less significant but still present at the $\sim 3\ \sigma$ level. The reasons for the differences may lie in the gas kinematics, or in the strength of the λ1600 feature that is probably dominated by Fe II emission. Both may play a part.

Another interesting correlation with log R (which is probably a measure of orientation of the central engine) is a signifi-

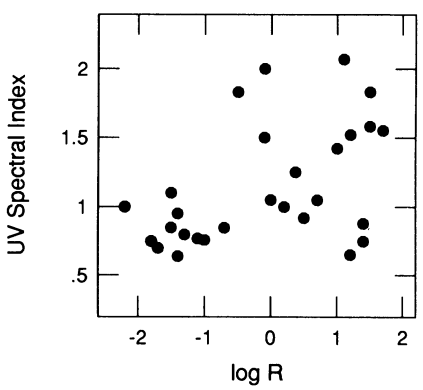

FIG. 5.—The ultraviolet spectral index, α_{UV} ($F_\nu \propto \nu^{-\alpha_{UV}}$) as a function of radio core dominance, log R.

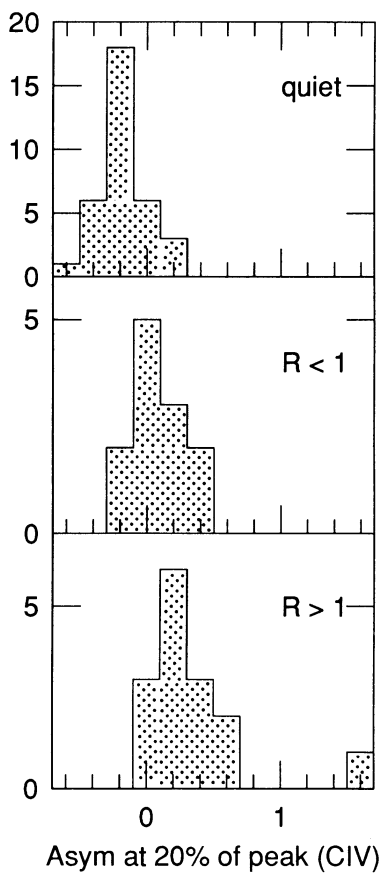

FIG. 6.—Histograms showing the significant differences in distributions of the asymmetry index for radio-quiet QSOs, core-dominant quasars ($R > 1$), and lobe-dominant quasars ($R < 1$).

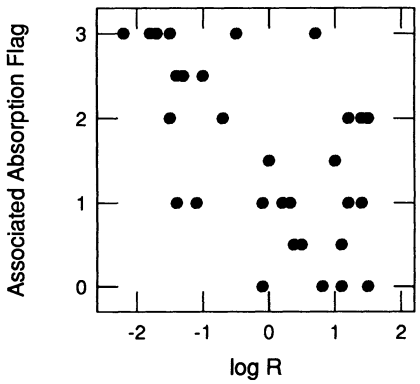

FIG. 7.—The strength of associated absorption as a function of radio core dominance, log R. Strength flag = 0 means no absorption was detected, and flag = 3 means the strongest absorption. The flags for Lyα and C IV have been averaged.

cant increase in strong associated absorption with decreasing log R—as if the absorption probability increases toward smaller "disk" latitudes (Student's $t = 3.7\ \sigma$; Fig. 7). This does not appear to be a result of associated absorption being easier to see in broader lines, as that correlation (absorption flag vs. FW50M) is much weaker (Student's $t = 2.2\ \sigma$). This relation ties in with the idea that associated absorption may be occurring in high-ionization material evaporated from a dusty torus (Voit, Weymann, & Korista 1993).

These trends will be discussed in more detail when we present the extension of these spectra to longer wavelengths.

Anne Kinney, George Hartig, Anuradha Koratka, Daniel Golombek, Tony Keyes, Jen Christiansen, and their colleagues at STScI suffered innumerable questions, and their patience is much appreciated. We also thank Buell Januzzi, Ari Laor, Barbara McArthur, and John Bahcall for help, advice and for supplying data before publication. We are very grateful to the Space Telescope Science Institute (STScI) for support under grant number HST GO-2578.01-87A RQ-Q. STScI is operated by AURA, Inc., under NASA contract NAS5-26555. We also thank the US-Israel Binational Science Foundation for support (BSF 8900179).

REFERENCES

Anderson, S. F. 1992, Faint Object Spectrograph Science Verification Report CAL/FOS-075 (Baltimore: STScI)
Ayres, T. R. 1993, Faint Object Spectrograph Science Verification Report CAL/FOS-115 (Baltimore: STScI)
Bahcall, J. N., et al. 1993, ApJS, 87, 1
Baldwin, J. A., Ferland, G. J., Carswell, R. F., Phillips, M. M., Wilkes, B., & Williams, R. E. 1993, in preparation
Bohlin, R. C. 1993, Faint Object Spectrograph Science Verification Report CAL/FOS-097 (Baltimore: STScI)
Bohlin, R. C., & Cox, C. 1992, HST Calibration Status Report (Baltimore: STScI)
Bohlin, R. C., & Neill, J. D. 1992, *HST* FOS Instrument Science Report No. 84 (Baltimore: STScI)
Brotherton, M. S., Wills, B. J., Francis, P. J., & Steidel, C. C. 1994, ApJ, 423, 131
Burstein, D., & Heiles, C. 1982, AJ, 87, 1165
Cardelli, J. A., Clayton, G. C., & Mathis, J. S. 1989, ApJ, 345, 245
Espey, B. R., Carswell, R. F., Bailey, J. A., Smith, M. G., & Ward, M. J. 1989, ApJ, 342, 666
Evans, I. N. 1993, Faint Object Spectrograph Science Verification Report CAL/FOS-107 (Baltimore: STScI)
Ferland, G. J., & Persson, S. E. 1989, ApJ, 347, 656
Ford, H. C., & Hartig, G. F. 1990, Faint Object Spectrograph Handbook, version 1.1 (Baltimore: STScI)
Francis, P. J., Hewett, P. C., Foltz, C. B., & Chaffee, F. H. 1992, ApJ, 398, 476
Hamann, F., & Ferland, G. J. 1993, ApJ, 418, 11
Jannuzi, B. T., & Hartig, G. F. 1994, in Proc. *HST* Calibration Workshop, ed. J. C. Blades (Baltimore: STScI), 215
Junkkarinen, V., et al. 1992, Faint Object Spectrograph Science Verification Rept. CAL/FOS-066 (Baltimore: STScI)
Keyes, C. D. 1994, in Proc. *HST* Calibration Workshop, ed. J. C. Blades (Baltimore: STScI), 138 & 209
Kinney, A. L. 1992, Faint Object Spectrograph Handbook, Version 2.0 (Baltimore: STScI)
Kinney, A. L., & Bohlin, R. C. 1993, Faint Object Spectrograph Science Verification Rept. CAL/FOS-103 (Baltimore: STScI)
Kinney, A. L., Huggins, P. J., Bregman, J. N., & Glassgold, A. E. 1985, ApJ, 291, 128
Kinney, A. L., Huggins, P. J., Glassgold, A. E., & Bregman, J. N. 1987, ApJ, 314, 145
Kondo, Y. 1987, in Exploring the Universe with the IUE Satellite, ed. Y. Kondo, W. Wamsteker, A. Boggess, M. Grewing, C. de Jager, A. L. Lane, J. L. Linsky, & R. Wilson (Dordrecht: Reidel), 1
Koratkar, A. 1994, FOS Calibration Manual (Baltimore: STScI)
Koratkar, A., & Taylor, C. J. 1993, Faint Object Spectrograph Science Verification Rept. CAL/FOS-096 (Baltimore: STScI)
Kriss, G. A., et al. 1992, ApJ, 392, 485
Kriss, G. A., Blair, W. P., & Davidsen, A. F. 1992, Faint Object Spectrograph Science Verification Report CAL/FOS-070 (Baltimore: STScI)
Laor, A., Bahcall, J. N., Jannuzi, B. T., Schneider, D. P., & Green, R. F. 1995, ApJ, in press
Laor, A., Bahcall, J. N., Jannuzi, B. T., Schneider, D. P., Green, R. F., & Hartig, G. F. 1994, ApJ, 420, 110
Lasker, B. M. 1990, AJ, 99, 2019
Lindler, D. J., & Bohlin, R. C. 1993, Faint Object Spectrograph Science Verification Report CAL/FOS-102 (Baltimore: STScI)
Lyons, R., Baity, W. A., Beaver, E. A., Cohen, R. D., Junkkarinen, V. T., & Linsky, J. B. 1992a, Faint Object Spectrograph Science Verification Report CAL/FOS-083 (Baltimore: STScI)
Lyons, R., Linsky, J. B., Beaver, E. A., Baity, W. A., & Rosenblatt, E. I. 1992b, Faint Object Spectrograph Science Verification Report CAL/FOS-080 (Baltimore: STScI)
Neill, J. D., Bohlin, R. C., & Hartig, G. 1992, Faint Object Spectrograph Science Verification Report CAL/FOS-077 (Baltimore: STScI)
Netzer, H. 1985, ApJ, 289, 451
Netzer, H., & Wills, B. J. 1983, ApJ, 275, 445
Netzer, H., Kazanas, D., Wills, B. J., Wills, D., Baldwin, J. A., Ferland, G. J., Han, M., Brotherton, M. S., & Browne, I. W. A. 1994, ApJ, 430, 191
Rees, M. J., Netzer, H., & Ferland, G. J. 1989, ApJ, 347, 640
Rosa, M. R. 1993, Faint Object Spectrograph Science Verification Report CAL/FOS-114 (Baltimore: STScI)
Sargent, W. L. W., Boksenberg, A., & Steidel, C. C. 1988, ApJS, 68, 539
Sargent, W. L. W., Steidel, C. C., & Boksenberg, A. 1989, ApJS, 69, 703
Taylor, C. J., & Keyes, C. D. 1993, Faint Object Spectrograph Science Verification Report CAL/FOS-000 (Baltimore: STScI)
Véron-Cetty, M.-P., & Véron, P. 1991, A Catalogue of Quasars and Active Nuclei, ESO Scientific Report No. 10 (5th ed.; Munich: ESO)
Voit, G. M., Weymann, R. J., & Korista, K. T. 1993, ApJ, 413, 95
Wilkes, B. J. 1984, MNRAS, 207, 73
Wills, B. J. 1991, in Variability of AGN, ed. H. R. Miller & P. J. Wiita (Cambridge: Cambridge Univ. Press), 87
Wills, B. J., & Browne, I. W. A. 1986, ApJ, 302, 56
Wills, B. J., Brotherton, M. S., Fang, D., Steidel, C. C., & Sargent, W. L. W. 1993b, ApJ, 415, 563
Wills, B. J., Hough, J. H., Bailey, J. A., & Wills, D. 1995, in preparation
Wills, B. J., Netzer, H., Brotherton, M. S., Han, M., Wills, D., Baldwin, J. A., Ferland, G. J., & Browne, I. W. A. 1993a, ApJ, 410, 534
Wills, B. J., Netzer, H., & Wills, D. 1980, ApJ, 242, L1
———. 1985, ApJ, 288, 94
Wills, B. J., Wills, D., Breger, M., Antonucci, R. R. J., & Barvainis, R. 1992, ApJ, 398, 454